

Enormous enhancement of resistivity in nanostructured electron-phonon systems

Debraj Bose, Sankha Subhra Bakshi and Pinaki Majumdar

Harish-Chandra Research Institute (A CI of Homi Bhabha National Institute), Chhatmag Road, Jhusi, Allahabad 211019

(Dated: August 23, 2024)

Recent experiments on nanoclusters of silver (Ag) embedded in a gold (Au) matrix reveal a huge increase in both the zero temperature resistivity and the coefficient of the “ T linear” thermal resistivity with increasing volume fraction of Ag. A fraction $f \sim 50\%$ of Ag leads to a factor of 20 increase in the residual resistivity, and a 40 fold enhancement in the coefficient of linear T resistivity, with respect to Au. Since Au and Ag both have weak electron-phonon coupling we surmise that the huge enhancements arise from a moderately large electron-phonon coupling that may emerge at the Ag-Au interface. We construct nanocluster configurations for varying f in two dimensions, define a Holstein model on it with weak coupling on the ‘interior’ sites and a strong coupling on the interfacial sites, and solve the model through exact diagonalisation based Langevin dynamics. Computing the resistivity, we observe a large $T = 0$ increase with f and also a linear T enhancement factor of ~ 30 . While the enhancement factors are parameter choice dependent, our key qualitative result is that the interface physics is inhomogeneous, with widely varying distortions, and different segments of the interface dictate the residual resistivity and the thermal scattering.

In the noble metals the resistivity around room temperature is dominated by electron-phonon scattering [1, 2]. The temperature dependence of resistivity takes the form $\rho(T) \sim \rho_0 + \delta\rho(T)$ where the residual resistivity ρ_0 in high purity samples is $\lesssim 0.1\mu\Omega\text{cm}$ [3], and the temperature dependence is $\delta\rho(T) \sim g^2T$, where g is the effective electron-phonon (EP) coupling [4]. In these materials g is small [5], and $\delta\rho(300K) \sim \text{few } \mu\Omega\text{cm}$ [3]. One may expect that nanohybrids of two such metals will have a similar $\delta\rho(T)$. Instead, recent experiments [6, 7] on clusters of Ag embedded in Au show that in a hybrid with 50 – 50 Ag-Au the linear T coefficient is 40 fold larger than that in Au nanoclusters!

‘Anomalous’ transport in electron-phonon systems has been known before, due to strong coupling or the presence of disorder. The simplest instance is deviation from linear T dependence of resistivity, with a reducing slope suggestive of resistivity saturation in strong coupling systems [8–11]. The next is polaron formation [12–18] and the emergence of a charge localised insulating phase. Finally, there are instances of disorder interplaying with strong EP coupling leading to deviations from Mathiessen’s rule, e.g. in A-15 compounds [19, 20]. Several attempts have been made to study the disordered strong coupling problem theoretically [21–23].

The Au-Ag nanohybrids share some similarities with the situations above but also major differences: (i) at large volume fraction of Ag in Au ($\sim 50 - 50$), one sees a sublinear T dependence of $\delta\rho(T)$ - the precursor of resistivity saturation. This is a ‘strong coupling’ signature. However, (ii) both Ag and Au are wide band metals with weak EP coupling and just a hybrid structure would not increase the EP coupling in the interior of the clusters. Any enhancement would be related to the interfaces. This situation we feel has both ingredients of (a) emergent strong coupling, and (b) disorder due to the presence of interfaces. In addition to transport measurements, the experiments confirmed the enhancement of effective EP coupling through point contact spectroscopy [7].

To model this nanohybrid system we envisage three kinds of sites. Two of these are ‘interior sites’: Au and Ag sites away

from the Au-Ag interface, while the third are Au or Ag sites at the interface. We assume that the interior sites would have electronic parameters mimicking bulk Au or Ag, while the interfacial sites would have different parameters altogether. On a given structural motif a fraction f would be Ag and $1 - f$ would be Au. Of the total number of sites a certain fraction I_f would be at the interface. Within a two dimensional (2D) Holstein model we assume that (i) the onsite potential of Au and Ag sites are equal (we change this later), (ii) all ‘interior’ sites (Ag or Au) have weak EP coupling g_1 , and (iii) Ag or Au sites at the interface have a larger EP coupling g_2 . We work at density $n = 0.25$ and use $g_1 = 0.2$ and $g_2 = 1.6$. The basis for choosing these numbers, and the effect of parameter variations is discussed later.

We generate structural motifs for varying volume fraction f via a simple algorithm described in the Supplement. We solve for the phonon distortions on these structures by using a Langevin equation [24–27] that iteratively diagonalises the electron problem and exactly handles strong EP coupling and thermal fluctuations. The distortion fields $x_i^\alpha(t)$, where \mathbf{R}_i is the site index, t is time, and α denotes an interface geometry, serve as the input to calculating electronic properties like resistivity and density of states.

Before studying the nanohybrid we computed $\rho(T)$ in the ‘clean’ problem for varying EP coupling - all the way from the weak coupling metal to the polaronic insulator. The results, and the ‘scaling’ that emerges for $\rho(T)$, serve as a template for analysing the clustered system. Our main results on the nanostructured problem are the following:

(i) *Nature of the interface*: Despite the same strong EP coupling on all interfacial sites the interface is very inhomogeneous, with wide variation in local density and associated lattice distortions.

(ii) *Residual resistivity*: The zero temperature resistivity ρ_0 arises from large distortions at a small fraction of the interfacial sites, which acts as effective ‘disorder’ seen by the electrons. ρ_0 does not increase linearly with I_f , particularly at large f .

(iii) *T linear coefficient and saturation:* The coefficient of T linear resistivity increases by a factor of 30 from the ‘pure Au’ limit to that of 50 – 50 Ag-Au. The experimental enhancement at 50 – 50 is ~ 40 [7]. $\delta\rho(T, f)$ plotted with respect to $A(f)T$ shows approximate collapse to a single sub-linear curve, suggestive of resistivity saturation at higher T , particularly at large f .

(iv) *Thermal scattering mechanisms:* The thermal scattering occurs due to lattice fluctuations around the $T = 0$ distortions. We find that at a given T low and high electron density sites on the interface have relatively small fluctuation while sites with intermediate density, $n_i \sim 0.6$, have far larger fluctuation. The $T = 0$ and finite T scattering sources are complementary.

Model and method: We study the 2D Holstein model on cluster motifs, defining a variable η_i such that for Au or Ag sites on the interface $\eta = 1$, while for sites away from the interface (i.e in the bulk) $\eta = 0$. Bulk sites have EP coupling g_1 while interfacial sites have EP coupling g_2 . We have $H = H_k + H_{ph} + H_{ep}$, with

$$H = -t \sum_{\langle ij \rangle} c_i^\dagger c_j + \sum_i \left(\frac{p_i^2}{2M} + \frac{Kx_i^2}{2} \right) - g_1 \sum_i (1 - \eta_i) n_i x_i - g_2 \sum_i \eta_i n_i x_i \quad (1)$$

We set $t = 1$ as the reference scale, $M = 25$, and $K = 1$. We comment later on the effect of a site potential difference between Au and Ag. The cluster configuration generating algorithm is described in the Supplement. Typical non overlapping clusters are 4×4 . At large coverage they begin to overlap.

To generate the equilibrium phonon configurations of H at some T on these motifs we use a Langevin equation, with thermal noise and a dissipation coefficient which satisfy the fluctuation-dissipation relation. Defining $H_{el} = H_k + H_{ep}$,

$$\begin{aligned} M \frac{d^2 x_i}{dt^2} &= -Kx_i(t) - \frac{\partial \langle H_{el} \rangle}{\partial x_i} - M\gamma \frac{dx_i}{dt} + \xi_i(t) \\ \frac{\partial \langle H_{el} \rangle}{\partial x_i} &= -(g_1(1 - \eta_i) + g_2\eta_i) \langle n_i \rangle \\ \langle n_i \rangle &= \sum_m |\psi_{im}|^2 n_f(\epsilon_m) \\ \langle \xi_i(t) \rangle &= 0, \quad \langle \xi_i(t) \xi_j(t') \rangle = 2\gamma k_B T \delta_{ij} \delta(t - t') \end{aligned} \quad (2)$$

We set the damping factor $\gamma = 0.2$. The ψ_{im} are site amplitudes of the instantaneous eigenvectors of H_{el} for a given $x_i(t)$ and ϵ_m are the corresponding eigenvalues. The Fermi factors $n_f(\epsilon_m)$ are used to calculate the occupation of the eigenstates. The non trivial part is calculating $\langle n_i \rangle$ since it requires diagonalising H_{el} for every move. This is prohibitive for large systems. We benchmark and use a scheme where $\langle n_i \rangle$ is computed by diagonalising H_{el} on an update cluster defined around the target site \mathbf{R}_i . This update cluster includes \mathbf{R}_i , its 4 nearest neighbours (NN), the 4 NNN, and the 4 axial sites beyond that. This cluster geometry, and benchmarks of the cluster scheme with respect to full diagonalisation, are

shown in the Supplement. The scheme allows us access to system size 30×30 .

Fig.1 shows our results on the resistivity $\rho(T)$ in the homogeneous problem (all $\eta = 0$) for varying $g_1 = g$. The Kubo formula for conductivity that we use is given in the Supplement. Our two dimensional ‘resistivity’ are in units of $\hbar/(\pi e^2)$. The main panel in Fig.1(a) shows $\rho(T, g)$, upto $g = 1.8$ and $T = 0.03$. Over a low T window $\rho(T)$ has a linear dependence on T in this classical phonon model, unlike the quantum problem where for $T \ll \theta_D$, the Debye temperature, it has a faster fall. With increasing T the resistivity shows a sublinear behaviour, which gets prominent with increasing g . The inset compares $\rho(T)$ in the metal at $g = 1.8$ and in the polaronic insulator at $g = 2$. We clearly see the $d\rho/dT \rightarrow 0$ behaviour at high T in the metal as well as the insulator. The presence of an insulating state shows why the metallic resistivity cannot keep indefinitely increasing with T and in this case would saturate to $\rho \sim 4$.

We tried a fit $\rho(T) = A(g)T - B(g)T^2$, over the $T = 0 - 0.03t$ window. The B coefficient reduces the rate of growth so we have used a negative sign. The dotted lines in Fig.1(a) show the fit of this form to $\rho(T, g)$. Fig.1(b) shows $A(g)$ and $B(g)$. Perturbation theory suggests that $A(g) \propto g^2$ and that the next order correction would be $B(g) \propto g^4$. The dot-

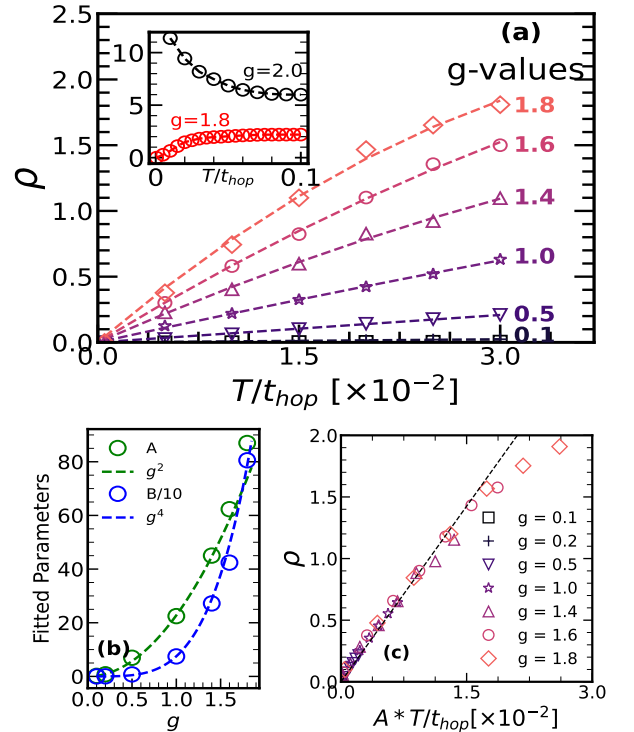


FIG. 1. Resistivity in the homogeneous problem for varying EP coupling g , at $n = 0.25$. (a) $\rho(T, g)$, with the dotted lines being fits of the form $A(g)T - B(g)T^2$. (b) The coefficients $A(g)$ and $B(g)$ fitted to power laws g^2 and g^4 , respectively. (c) Plot of $\rho(T, g)$ with respect to $A(g)T$. There is no perfect scaling collapse, but a rough sublinear trend.

ted lines are reasonable fits using these power laws. Fig.1(c) shows $\rho(T, g)$ plotted with respect to $A(g)T$. Due to the differing g dependence of the A and B coefficients there is no ‘scaling collapse’, but instead a g dependent downward bend. However, upto $g = 1.6$, and for the low T probed, there is a rough sublinear collapse.

Cluster configuration and distortions: The top row in Fig.2 shows the interface in single copies of samples with $f = 0.1, 0.3, 0.5$, marked out in red (the large g sites) and the interior of the Ag clusters marked in silver. The middle row shows the electron density n_i at $T = 0$ in these configurations. While all large n_i sites are on the interface, not all interfacial sites have large n_i . In fact the density at interfacial sites ranges from $n \sim 0.2$ (as in the ‘bulk’) all the way to $n \sim 0.8$. Had the large g sites been *isolated* they would all have had large n_i . This n_i , and the associated $T = 0$ distortion field x_i^0 , will be the source of scattering and residual resistivity.

The bottom row shows the spatially resolved amplitude of mean square thermal fluctuation $(\Delta x_i)^2 = \langle (\delta x_i)^2 \rangle$ at $T = 0.01t$, where $\delta x_i = x_i - x_i^0$. Again, the large Δx_i sites are all on the interface, but these are only a fraction of interfacial sites. Further, sites with large (or small) n_i actually have much smaller Δx_i than sites with $n_i \sim 0.6$. The thermal scattering, that leads to the enhanced T linear slope, will be dominated by the medium x_i^0 sites on the interface. All these puts paid to the expectation that an interface of length I_f and large EP coupling g_2 would lead to thermal scattering $\propto g_2^2 I_f$. We look next at the resistivity and then try to relate it to x_i^0 and Δx_i .

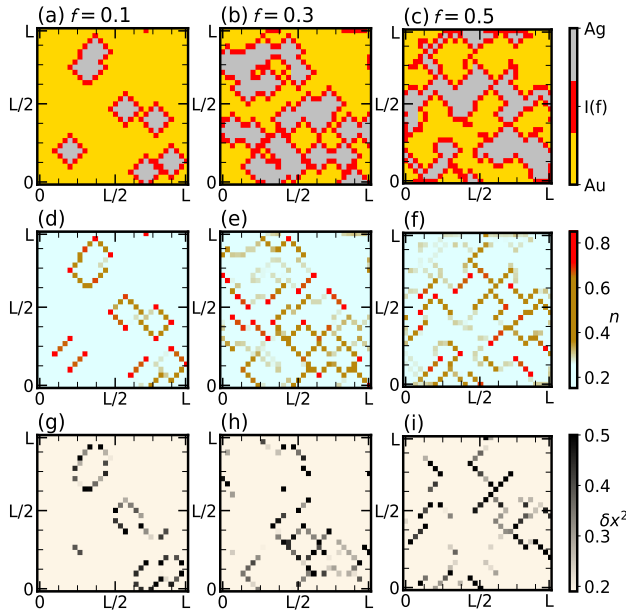


FIG. 2. Interfaces, and spatial character of distortions at $f = 0.1, 0.3, 0.5$. Top: the ‘boundary sites’ with EP coupling g_2 . Middle: Map of density n_i at $T = 0$. Bottom: Map of mean square fluctuation $(\Delta x_i)^2 = \langle (\delta x_i)^2 \rangle$ at temperature $T = 0.01t$. Note that all large g locations do not have large n_i , and that large n_i and large $(\Delta x_i)^2$ are actually anticorrelated.

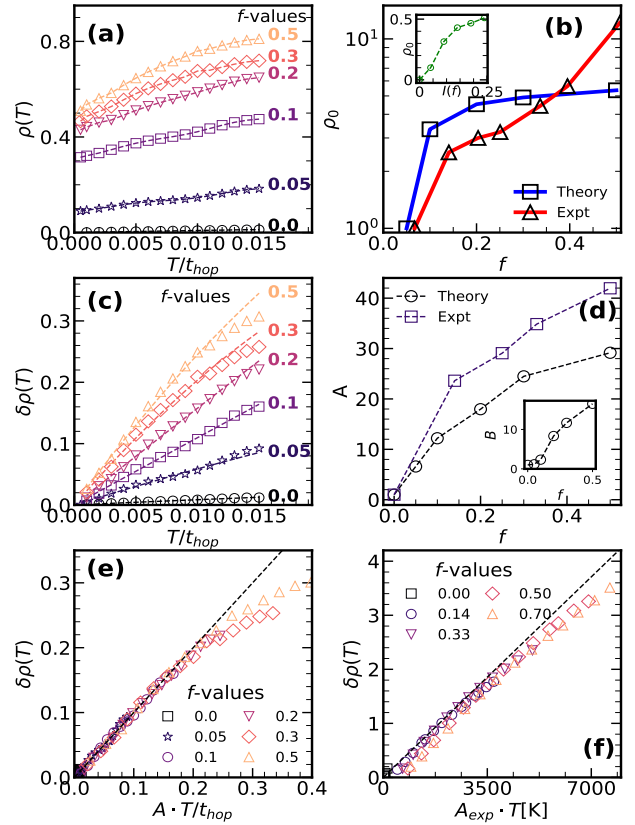


FIG. 3. Resistivity with varying Ag concentration, f . (a) The total resistivity $\rho(T, f) = \rho_0(f) + \delta\rho(T, f)$, on 30×30 lattices, averaged over 10 cluster configurations. (b) The residual resistivity, normalised by it’s value at $f = 0.05$, comparing our result with experimental data. The inset shows that our residual resistivity is not simply proportional to the perimeter I_f . (c) Our result on $\delta\rho(T)$ for different f , note the sublinear growth at large f . We fit $\delta\rho(T, f) = A(f)T - B(f)T^2$ (dotted lines). (d) $A(f)$, the slope of the linear T part of our $\delta\rho(T, f)$, normalised by it’s value at $f = 0$, and the corresponding result from experiment. The inset shows our $B(f)$. (e) Plot of our $\delta\rho(T, f)$ with respect to $A(f)T$. (f) The experimental result corresponding to panel (e).

Resistivity: Fig.3(a) show the resistivity $\rho(T, f)$ that we obtain by generating x_i configurations on a 30×30 lattice and averaging the conductivity thermally and over 10 cluster configurations. The data is plotted to $T = 0.015t$ and shows both the increase in ρ_0 with f and the less prominent increase in the slope of $\delta\rho(T)$. Fig.3(b) superposes our $\rho_0(f)$ with that obtained from experiments, both results being normalised to the value at $f = 0.05$. Beyond $f \sim 0.3$ the experimental ρ_0 has a stronger growth than the theory result. Note that our $f = 0$ result has zero resistivity, unlike the experiment. Our $\rho_0(f)$ does not vary linearly with I_f at large f (inset).

Fig.3(c) shows the thermal component of $\rho(T)$ that we obtain. While the coupling constants g_1 and g_2 are now fixed we can try a fit $\delta\rho(T, f) = A(f)T - B(f)T^2$. The corresponding fits are superposed on the data points. Like in the ‘clean problem’ in Fig.1 we see a slope increasing with f and

also sublinear behaviour at large T . Fig.3(d) shows the coefficient $A(f)$, normalised by $A(0)$, comparing our result with experiments. The amplification factor at $f = 0.5$ is ~ 40 experimentally, while for us it is ~ 30 . This number depends on the choice of g_2 , as we comment on in the Supplement. The behaviour of our $B(f)$ is shown in the inset to Fig.3(d).

Fig.3(e) plots our $\delta\rho(T, f)$ with respect to $A(f)T$. It shows the deviation from a linear scaling curve at large f and high T . Fig.3(f) shows the corresponding scaling curve from experiments.

Relation between structural distortions and resistivity: We take a look at the distribution of structural distortions both at zero and finite T and then attempt to relate the distortions to the resistivity. Fig.4 looks at the phonon properties in a particular cluster configuration at $f = 0.3$. Panel (a) looks at the spatial map of $T = 0$ distortions x_i^0 . We use a ‘four color’ map, identifying distortions as large (red), medium (magenta), small (gold) or very small (white). Note that at $T = 0$ the distortions and local density are related by $x_i^0 = (g_i/K)n_i$, obtained simply by minimising H_{el} with respect to x_i^0 .

The distribution of $T = 0$ distortion: $P(x) = (1/N) \sum_i \delta(x - x_i^0)$ is shown in panel (b). The continuous values of x_i^0 are retained but the features are coloured according to our large-medium-small scheme. A very large fraction of sites, $\sim (1 - I_f)$, have small distortions since the corresponding $g = g_1$. The interfacial sites, all with $g = g_2$, have the I_f fraction distributed as shown. These x_i^0 , which are already proportional to the respective g_i , gen-

erate the $T = 0$ scattering potential $V_0^i = g_i x_i^0$ that decides the residual resistivity. We show the distribution $P(V_0, f) = (1/N) \sum_i \delta(V_0 - g_i x_i^0)$ in the Supplement.

Fig.4(a) also marks out three ‘typical’ sites, 1, 2, 3, where we want to probe thermal fluctuations. We examine the time series $x_i(t)$ at these sites at different temperatures and construct the distribution of fluctuations: $P_i(\delta x) = (1/N_\tau) \sum_\tau \delta(\delta x - (x_i - x_i^0))$, Fig.4(c), where N_τ is the number of thermal samples. The thermal scattering would arise from the ‘disorder’ $V_{th}^i = g_i^2 (\Delta x_i)^2$, where $(\Delta x_i)^2$ is the variance of $P_i(\delta x)$ defined earlier. Note that at site 1 - a medium density site - the width of $P_i(\delta x)$ is more than twice the value at sites 1 and 3.

Fig.4(d) shows that at all the sites the width $(\Delta x_i)^2 \propto T$. The nature of thermal fluctuations is consistent with a local density dependent phonon stiffness K_i which is close to the bare value for $n_i \sim 0, 1$ and is significantly smaller for $n_i \sim 0.6$. In the Supplement we show a simple perturbative calculation, using $P(V_0, f)$ and the thermal fluctuation $\Delta x_i(T)$, to explain the ρ_0 and the linear T slope.

On the whole, the residual resistivity arises primarily from the large x_i^0 sites at the interface, while the thermal scattering is dominated by the medium density sites at the interface.

Discussion: (i) Effect of electronic parameter variation: The g_1 value used in our calculation should correspond to bulk Au in the 3D Holstein model. We found the 3D value to be ~ 0.3 (see Supplement). Given the smaller coupling window for metallicity in 2D (limited by polaron formation) we used the slightly lower value, $g_1 = 0.2$. The g_2 value is limited by the polaronic instability which occurs around $g \sim 2$ in 2D. We have explored $g_2 = 1.4, 1.6$ and find a rapid variation, faster than g_2^2 , in the linear T coefficient. Our g_2 value is mainly to demonstrate a qualitative effect. We have also checked the effect of a higher site potential on Ag sites so that there is a higher electron density in the Au region. It does not make much difference as long as g_1 and g_2 are kept as before. The results are in the Supplement.

(ii) The possible origin of large interfacial EP coupling: We have made no suggestions on the physical mechanism that could generate a large g_2 , and have only addressed the consequences of such a coupling. Addressing this requires modeling the local chemistry of the Ag-Au system, including the local potentials involved, and possible Ag to Au charge transfer. This has been attempted [7], at the level of a model Hamiltonian, in the experimental paper itself. Their result, at small charge transfer δn , extrapolated to realistic δn , suggests that an EP coupling consistent with resistivity amplification might be achievable. This, however, is an averaged, homogeneous, conception of the EP coupling, while we find that even the interface is a spatially differentiated object. A meaningful exploration of nanohybrids would involve DFT calculations to set local parameters and then many body schemes for transport and collective effects.

(iii) Possible superconductivity: since there is an enhanced, albeit inhomogeneous, EP coupling in the system, larger than what obtains in superconducting elements like Pb, Hg, or

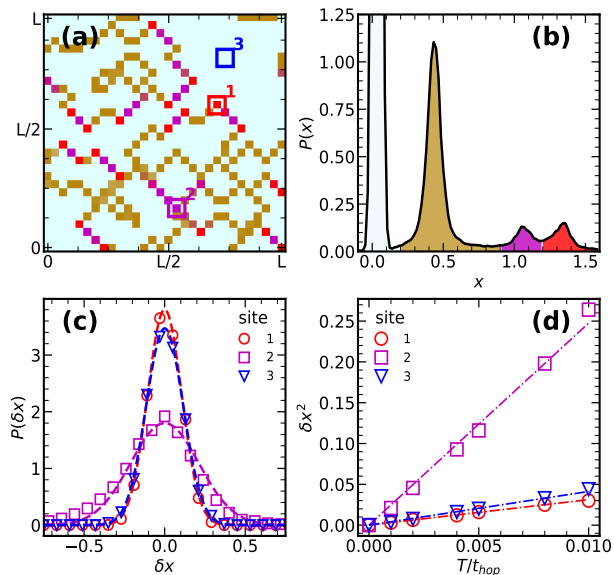


FIG. 4. Phonon distortions and local spectra at $f = 0.3$, single copy data. (a) Map of the $T = 0$ distortion x_i^0 . (b) The distribution $P(x)$ of distortions at $T = 0$. (c) The local distributions $P_i(\delta x)$, where $\delta x_i = x_i - x_i^0$ at 3 sites (marked in (a)) at $T = 0.01t$. (d) The T dependence of the on site variance $(\Delta x_i)^2$ at the three sites marked out in panel (a). All of them are $\propto T$, but the slope in the medium density site is much greater than that in the large and small density sites.

compounds like Nb_3Sn [5], one may ask whether this could lead to phonon induced superconductivity. Our treatment of phonons is classical, but once a $T = 0$ distortion field x_i^0 is obtained one can construct a harmonic quantum theory of the phonons. The associated phonon propagator $D_{ij}(\omega)$ could in principle mediate pairing but the strong disorder in the background needs to be considered in any theory of superconductivity. In addition if there are Coulombic effects in the real nanohybrid, due to charge transfer, that too needs to be built in. A periodic nanohybrid configuration may be a better candidate for superconductivity.

Conclusions: We constructed a electron-phonon model to address the huge resistivity amplification recently seen in Au-Ag nanohybrids. After generating cluster motifs appropriate to volume fractions f of Ag in Au, we defined a model that has low electron-phonon coupling in the ‘bulk’ and a large coupling on interfacial sites. We used an exact diagonalisation based Langevin scheme to handle the electron-phonon coupling and thermal fluctuations. For our choice of bulk and interfacial coupling we obtained a thermal resistivity amplification that is consistent with experiments in both its volume fraction dependence and overall magnitude. More importantly we find that while the interface is the crucial player in electron scattering, the dominant contributions to residual resistivity and thermal resistivity come from different spatial regions of the interface. Combined with first principles estimate of a few electronic parameters in the nanohybrid, our approach is capable of predicting the novel transport features and possible superconducting instabilities in these systems.

Acknowledgments: We acknowledge use of the HPC clusters at HRI. PM thanks Arindam Ghosh for sharing and discussing the experimental results.

-
- [1] J. M. Ziman, *Electrons and phonons*, Oxford University Press (1960).
- [2] P. B. Allen, Chapter 6, “Electron transport” in *Contemporary Concepts of Condensed Matter Science*, Volume 2, 2006, Pages 165-218.
- [3] Nguyen Quang Hoc, Bui Duc Tinh and Nguyen Duc Hien, *Influence of temperature and pressure on the electrical resistivity of gold and copper upto 1350K and 100 GPa*, *Materials Res Bulletin*, 128 (2020) 110874.
- [4] In the literature a dimensionless coupling $\lambda \propto g^2$ is often called the electron-phonon coupling. We use g^2 since g will be the electron-phonon coupling strength in our Holstein model.
- [5] P. B. Allen, *Electron-phonon coupling constants*, in Chapter 7 of *Handbook of Superconductivity*, edited by Charles P. Poole, Jr. Academic Press (2000).
- [6] Tuhin Kumar Maji, Shreya Kumbhakar, Binita Tongbram, T. Phanindra Sai, Saurav Islam, Phanibhushan Singha Mahapatra, Anshu Pandey, and Arindam Ghosh, *Electrical resistance in a composite of ultra-small silver nanoparticles embedded in gold nanostructures: implications for interface-enabled functionality*, *ACS Appl. Electron. Mater.* 2023, 5, 2893–2901.
- [7] Shreya Kumbhakar, Tuhin Kumar Maji, Binita Tongbram, Shinjan Mandal, Shri Hari Soundararaj, Banashree Deb-nath, T. Phanindra Sai, Manish Jain, H. R. Krishnamurthy, Anshu Pandey, and Arindam Ghosh, *Engineering ultra-strong electron-phonon coupling and nonclassical electron transport in crystalline gold with nanoscale interfaces*, [arXiv:2405.14684](https://arxiv.org/abs/2405.14684).
- [8] P. B. Allen, in *Superconductivity in D- and F-Band Metals*, Edited by H. Suhl and M. B. Maple, Academic Press, 1980; pp 291–304.
- [9] A. J. Millis, Jun Hu, and S. Das Sarma, *Resistivity saturation revisited: results from a dynamical mean field theory*, *Phys. Rev. Lett.* 82, 2354 (1999).
- [10] O. Gunnarsson, M. Calandra, J. Han, *Colloquium: Saturation of electrical resistivity*, *Reviews of Modern Phys.* 2003, 75, 1085.
- [11] M. Calandra, O. Gunnarsson, *Saturation of electrical resistivity in metals at large temperatures*, *Phys. Rev. Lett.* 2001, 87, 266601.
- [12] For a general reference see, e.g., A. S. Alexandrov and N. F. Mott, *Polarons and Bipolarons*, World Scientific, Singapore 1995.
- [13] Cesare Franchini, Michele Reticcioli, Martin Setvin and Ulrike Diebold, *Polarons in materials*, *Nature Reviews Materials*, 6, 560–586 (2021).
- [14] Aldo H. Romero, David W. Brown, and Katja Lindenberg, *Polaron effective mass, band distortion, and self-trapping in the Holstein molecular-crystal model*, *Phys. Rev. B* 59, 13728 (1999).
- [15] J. Bonca, S. A. Trugman, and I. Batistic, *Holstein polaron*, *Phys. Rev. B* 60, 1633 (1999).
- [16] S. Ciuchi, F. de Pasquale, S. Fratini, and D. Feinberg, *Dynamical mean-field theory of the small polaron*, *Phys. Rev. B* 56, 4494 (1997).
- [17] A. J. Millis, R. Mueller and B. I. Shraiman, *Fermi-liquid-to-polaron crossover. I. General results*, *Phys. Rev. B*, 54 (1996) 5389.
- [18] B. Poornachandra Sekhar, Sanjeev Kumar and Pinaki Majumdar, *The many-electron ground state of the adiabatic Holstein model in two and three dimensions*, *Europhys. Lett.*, 68 (4), 564 (2004).
- [19] L. R. Testardi, J. M. Poate, and H. J. Levinstein, *Anomalous electrical resistivity and defects in A – 15 compounds*, *Phys. Rev. B* 15, 2570 (1977).
- [20] H. Wiesmann, M. Gurvitch, A. K. Ghosh, H. Lutz, O. F. Kammerer, and Myron Strongin, *Estimate of density-of-states changes with disorder in A – 15 superconductors*, *Phys. Rev. B* 17, 122 (1978).
- [21] David Emin and M.-N. Bussac, *Disorder-induced small-polaron formation*, *Phys. Rev. B* 49, 14290 (1994)
- [22] Sanjeev Kumar and Pinaki Majumdar, *Singular effect of disorder on electronic transport in strongly coupled electron-phonon systems*, *Phys. Rev. Lett.* 94, 136601 (2005)
- [23] S. Ciuchi, D. DiSante, V. Dobrosavljevic, S. Fratini, *The origin of Mooij correlations in disordered metals* *npj Quantum Mater.* 2018, 3, 44.
- [24] D. Mozysky, M. B. Hastings, and I. Martin, *Intermittent polaron dynamics: Born-Oppenheimer approximation out of equilibrium*, *Phys. Rev. B* 73, 035104 (2006).
- [25] Jing-Tao Lü, Mads Brandbyge, Per Hedegard, Tchavdar N. Todorov, and Daniel Dundas, *Current-induced atomic dynamics, instabilities, and Raman signals: Quasiclassical Langevin equation approach*, *Phys. Rev. B* 85, 245444 (2012).
- [26] Sauri Bhattacharyya, Sankha Subhra Bakshi, Samrat Kadge, and Pinaki Majumdar, *Langevin approach to lattice dynamics in a charge-ordered polaronic system*, *Phys. Rev. B* 99, 165150

(2019).

- [27] Sauri Bhattacharyya, Sankha Subhra Bakshi, Saurabh Pradhan, and Pinaki Majumdar, *Strongly anharmonic collective modes in a coupled electron-phonon-spin problem*, [Phys. Rev. B 101, 125130 \(2020\)](#).

Supplementary to ‘Enormous enhancement of resistivity in nanostructured electron-phonon systems’

I. GEOMETRY OF THE AU-AG NANOSTRUCTURES

Generating cluster motifs

Consider a square lattice with $L \times L$ sites of gold atoms (Au). Silver (Ag) atoms replace some of the gold in this matrix. The presence of gold or silver at a site is represented by η_i , a binary field: $\eta_i = 0$ for gold and $\eta_i = 1$ for silver. In the clean limit $\eta_i = 0$ throughout the lattice. For a finite fraction f , we randomly select ζ sites (located at \vec{R}_{ζ_i}) and create a circular region around each of them with radius 2 (in units of lattice spacing). Within each of these regions, the field η_i is set to 1. The circles may overlap, and the fraction f is given by $(1/L^2) \sum_i \eta_i$. We define the boundary gold atoms surrounding these islands as the interface sites. Everywhere else, the value of $g_i = g_1$ while at the interface sites $g_i = g_2$. In Fig.1 we show three Au-Ag nanostructures each for three filling fractions f on a 30×30 lattice.

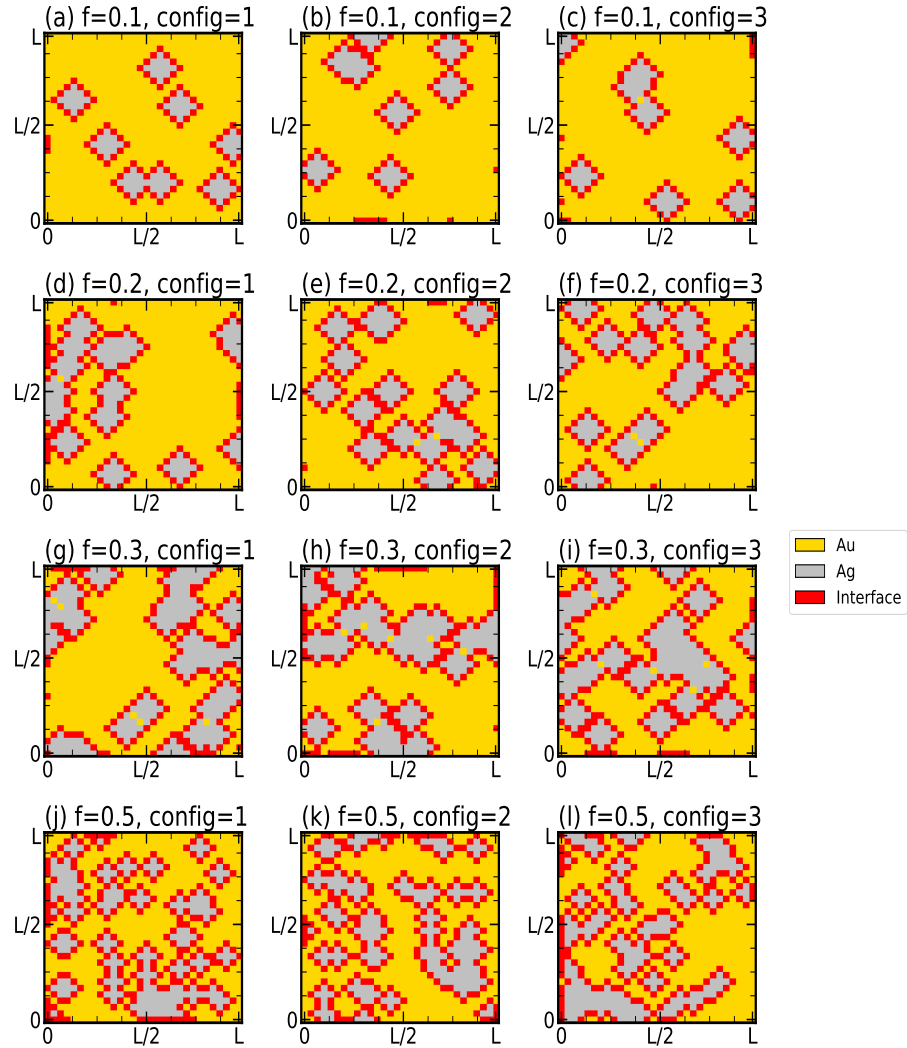


FIG. 1. Various configuration maps η_i for each filling fraction f (along the rows) and for different filling fractions f (along the column)

Interface length

The fraction of interfacial sites I_f increase with filling fraction f upto $f = 0.5$. The relationship between I_f and f in the non-overlapping regime (where the silver droplets are far away from each other, i.e. small f regime) is $I(f) = \frac{Z}{A}f$ where, Z is the number of interfacial sites in a single cluster and A is number of silver sites inside the cluster. For larger f , the droplets starts to overlap and this equation overestimates the $I(f)$. This relationship between I_f and f , averaged over 15 configurations is shown in Fig.2.

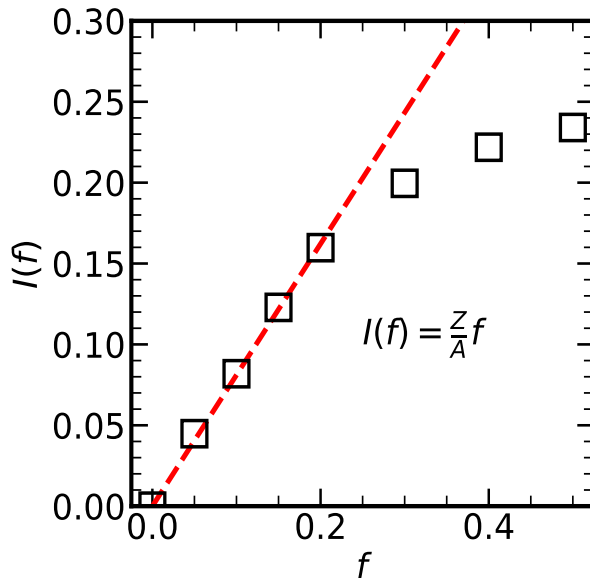


FIG. 2. relationship between $I(f)$ and f averaged over 15 configurations

II. BENCHMARKING CLUSTER BASED LANGEVIN UPDATE WITH EXACT DIAGONALIZATION

To generate the phonon configurations x_i , an exact diagonalization-based Langevin scheme can be employed. The primary computational challenge lies in calculating the force $\langle \partial H / \partial x_i \rangle$, which requires the diagonalization of an $N \times N$ matrix, where N is the total number of sites. This process scales as $\mathcal{O}(N^3)$. The computational cost can be reduced by considering a smaller cluster centered around the site and replacing $\langle \partial H / \partial x_i \rangle$ with $\langle \partial H / \partial x_i \rangle_C$, where the force is calculated using the cluster C surrounding the i -th site. It is important to note that in this context, the term "cluster" refers to a local neighborhood.

In our calculations, we use a cluster consisting of $N_c = 13$ sites. This cluster includes the site i , its 4 nearest neighbors (NN), the 4 next-nearest neighbors (NNN), and the 4 axial sites beyond them. We define a Hamiltonian H_C on this cluster with open boundary conditions and diagonalize it to compute the force on x_i . This force is then used in the Langevin equation to generate the equilibrium configurations x_i . When calculating electronic properties, we employ a full diagonalization method.

In Fig.3, we compare the distribution function $P(x)$ obtained from both the cluster-based and exact diagonalization-based Langevin dynamics in the homogeneous case, where the electron-phonon coupling g is uniform across all sites. We also investigate the effect of varying temperature. The results demonstrate that the cluster-based Langevin dynamics closely matches the outcomes of the exact diagonalization-based approach.

III. ESTIMATION OF g_1 FOR GOLD

To estimate the value of g_1 , we begin by considering the resistivity of gold (Au) at 300 K, which is approximately $2 \mu\Omega\text{-cm}$. From perturbative theory, the resistivity as a function of temperature is given by:

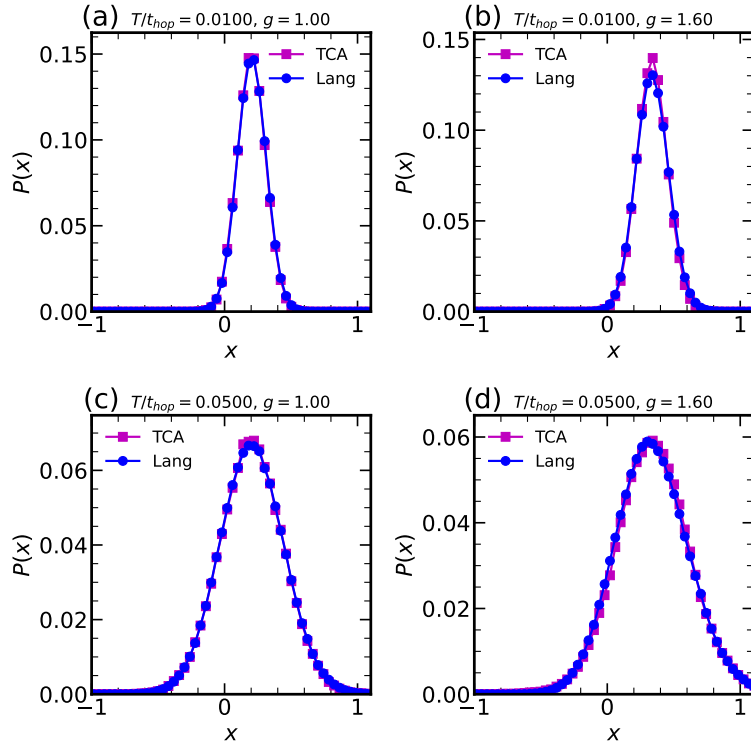


FIG. 3. Benchmark of cluster-based $P(x)$ vs x at two temperatures and two values of g with respect to full Langevin calculation on a 20^2 lattice. The panels correspond to: (a) $T/t_{hop} = 0.0100$, $g = 1.00$; (b) $T/t_{hop} = 0.0100$, $g = 1.60$; (c) $T/t_{hop} = 0.0500$, $g = 1.00$; (d) $T/t_{hop} = 0.0500$, $g = 1.60$.

$$\rho(T) = \rho_0 \cdot A \cdot g^2 \cdot \frac{T}{t_{hop}}$$

where $\rho_0 = \frac{\hbar a_0}{\pi e^2}$ is a characteristic resistivity, and $A \cdot g^2 \cdot \frac{T}{t_{hop}}$ is dimensionless. The proportionality constant A can be determined from a previous work (Phys. Rev. Lett. 94, 136601 (2005)) on disordered Holstein models, where for $g = 1$, it was found that $\rho(T) = 4\rho_0$ at $T = 0.3t_{hop}$. Thus, $A = \frac{4}{0.3} \approx 13$. For gold, with $a_0 = 4 \text{ \AA}$, $\rho_0 \approx 50 \mu\Omega\text{-cm}$. Substituting into the resistivity equation, we have:

$$50 \cdot 13 \cdot g_1^2 \cdot \frac{300}{t_{hop}} = 2$$

Solving for g_1^2 gives:

$$g_1^2 = \frac{t_{hop}}{98000}$$

Assuming a rough estimate for the bandwidth $t_{hop} \approx 10000 \text{ K}$ from band structure, we find:

$$g_1^2 \approx \frac{1}{10} \quad \text{or} \quad g_1 \approx 0.3$$

This value of g_1 is appropriate for a 3D system, where the critical coupling for polaron formation is higher than in 2D. For comparison, in 2D, $g_1 \approx 0.2$ would be reasonable, as we consider limiting g_2 to around 1.6.

IV. CHARACTERISING THE PHONON DISTORTIONS

In Fig. 4, we present the density map n_i^0 [4(a)-(c)], corresponding distributions $P(n)$ [4(d)-(f)], lattice distortion field x_i^0 [4(g)-(i)], and its distribution $P(x)$ [4(j)-(l)] at $T/t_{hop} = 10^{-5}$, along with the time-averaged map $(\delta x_i)^2$ [4(m)-(o)].

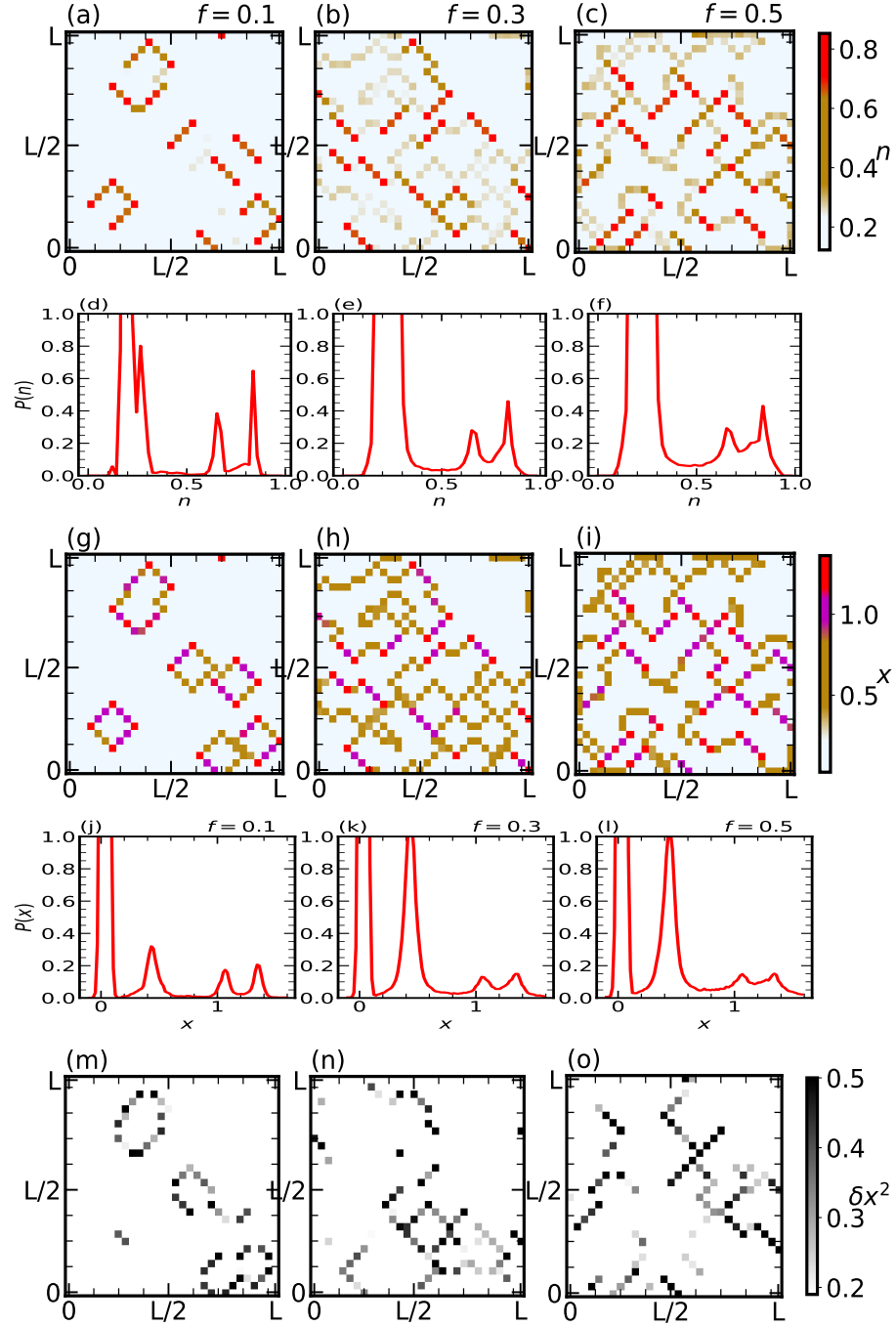


FIG. 4. Density map n_i^0 [4(a)-(c)], corresponding distributions $P(n)$ [4(d)-(f)], lattice distortion field x_i^0 [4(g)-(i)], its distribution $P(x)$ [4(j)-(l)] at $T/t_{hop} = 10^{-5}$, and time-averaged map $(\delta x_i)^2$ [4(m)-(o)] at higher T .

When we plot the low temperature ($T/t_{hop} = 10^{-5}$) distribution of the densities on the sites i where $i \in \{\text{interface}\}$ we see this distribution function shows a distinct three peak structure as shown in Fig. 5(a). These tri-modal structure can be fitted with a three Gaussian distributions of different widths and peak locations. The weight of these three separate peaks are I_{low} , I_{mid}

and I_{high} corresponding to the density values low, medium and high. upon changing the f , the total number of interfacial sites $I(f)$ also changes. To answer how does the I_{low} , I_{mid} and I_{high} changes as function of f , we plot them in Fig. 5(b).

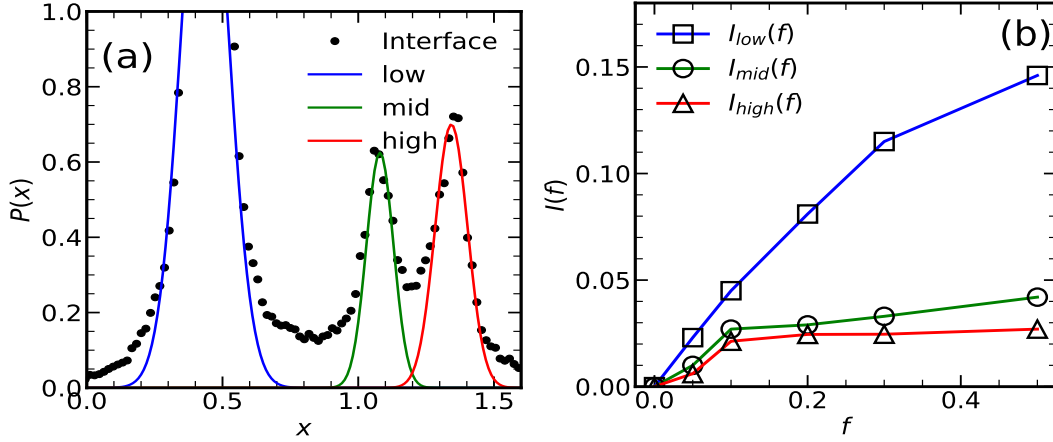


FIG. 5. The distribution of site densities at the interface exhibits a distinct tri-modal structure, as shown in Fig. 5(a), which can be fitted with three Gaussian distributions of varying widths and peaks. In Fig. 5(b), we plot the evolution of the weights I_{low} , I_{mid} , and I_{high} of these peaks as a function of f .

V. AVERAGING CONDUCTIVITY OVER CONFIGURATIONS

To calculate the conductivity, we assume a separation of time scales between charge and phonon dynamics. For an instantaneous background $\{x_i\}$, we diagonalize the single particle Hamiltonian as described in the main text. This yields the eigenfunctions ($f_{i,\epsilon}$) and eigenvalues (ϵ_n). The current operator is defined as $j_{mn}^x = \langle m | \hat{j}_x | n \rangle$. The conductivity is then computed as follows:

$$\sigma(\omega) = \sum_{m \neq n} \frac{|j_{mn}^x|^2}{\epsilon_m - \epsilon_n} \delta(\omega - (\epsilon_n - \epsilon_m)) [f_{\epsilon_m}(T) - f_{\epsilon_n}(T)], \quad (3)$$

where $f_{\epsilon}(T)$ denotes the Fermi function.

The D.C. conductivity $\sigma(\omega \rightarrow 0, T)_{\{x_i^\alpha\}}$ depends on the specific configuration $\{x_i^\alpha\}$, where α denotes different possible realizations of electron-phonon coupling matrix g_i for a given silver-to-gold ratio f . These configurations can vary because the local couplings g_i^α are generated in different ways. In Fig. 5, we plot the D.C. conductivity for various configurations. We then average the D.C. conductivity over all configurations (indicated by the black dotted line) to obtain a representative value. The resistivity, shown in the inset, is calculated as the inverse of this averaged conductivity.

VI. PERTURBATIVE ANALYSIS OF RESISTIVITY

Calculation for zero-temperature resistivity ρ_0

The resistivity ρ_0 arising from the 2nd-order perturbation theory can be set up if we consider the effect of phonons in zero-temperature as a disorder problem. The effective disorder potential V_i can be $-g_i x_i$. The x_i shows a distinct 4 peak features: 1 peak coming from the bulk, valued around $\sim -g_1^2/K$ (a small number compared to other cases), 3 other peaks arising from the interfacial sites: low (l), medium (m) and high (h) values of x . The probability distribution can be approximated as

$$P(x) = (1 - I(f))\delta(x - x_{bulk}) + I_\alpha \delta(x - x_\alpha) \quad (4)$$

where $I(f)$ is the number of interfacial sites and I_α denotes the three peaks among those such that $I(f) = \sum_\alpha I_\alpha$, $\alpha = \{l, m, h\}$.

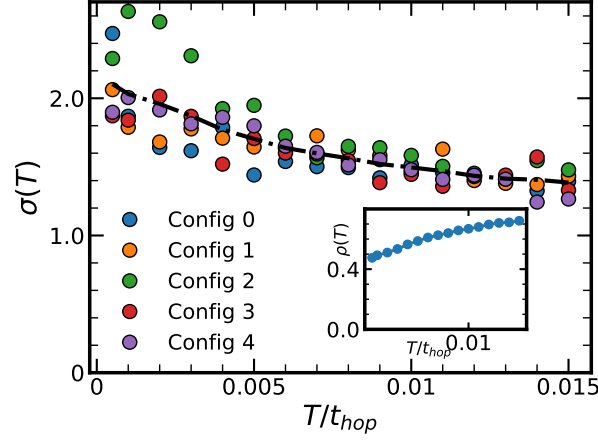


FIG. 6. D.C. conductivity σ as a function of temperature T for several configuration corresponding to different realization of same f on a 30×30 lattice. The dotted line shows their average. The plot in the inset shows the D.C. resistivity $\rho(T) = 1/\sigma(T)$

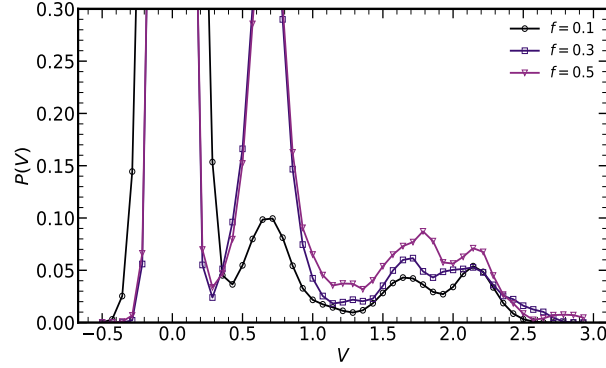


FIG. 7. $P(V)$ for 3 different values of f at $T = 10^{-5}t_{hop}$, where V is the potential. We approximate this with 4 delta functions corresponding to different peaks.

The average potential can be written as

$$\bar{V} = \int V P(V) dV \quad (5)$$

$P(V)$ is probability of finding a site with V value of potential. In this 4-delta-function approximated x distribution we have

$$\bar{V} = P_{bulk} V_{bulk} + \sum_{\alpha} I_{\alpha} V_{\alpha} \quad (6)$$

where $V_{bulk} = -g_1 x_{bulk}$ and $V_{\alpha} = -g_2 x_{\alpha}$.

The resistivity ρ from second order perturbation is proportional to

$$\rho_0 \propto \langle \Delta V^2 \rangle \quad (7)$$

And we notice,

$$\langle V^2 \rangle = \int dV V^2 \sum_{\alpha} I_{\alpha} \delta(V - V_{\alpha}) = \sum_{\alpha} I_{\alpha} V_{\alpha}^2 \quad (8)$$

and

$$\langle \bar{V} \rangle^2 = \left(\sum_{\alpha} I_{\alpha} \bar{V}_{\alpha} \right)^2 = \sum_{\alpha} I_{\alpha}^2 \bar{V}_{\alpha}^2 \quad (9)$$

Ignoring $g_1 x_1^2$ we get,

$$\rho_0 \propto \langle \Delta V^2 \rangle = g_2^2 [x_l^2 (I_l - I_l^2) + x_m^2 (I_m - I_m^2) + x_h^2 (I_h - I_h^2)] \quad (10)$$

Linear dependence of $\delta\rho$ on T

Now we consider the effect of temperature on resistivity by assuming that the distortions x_i can fluctuate around their $T = 0$ value x_i^0 . This results in a broader distribution around the peaks. This broadening of the distribution $P(\delta x)$ is shown in Fig.4(c) of the main paper where we plotted data for 3 sites in $P(\delta x)$, and we find that the standard deviation of sites corresponding to x by a factor of almost 6 for the middle-density site ($\alpha = m$), whereas it remains the same for the small-density ($\alpha = l$) or large-density sites ($\alpha = h$). This changes the resistivity as

$$\rho(T) \sim \rho_0 + \delta\rho(T) \quad (11)$$

We use this information in $\delta\rho(T)$ to estimate the A coefficient using this perturbative technique.

In a similar way we now calculate the resistivity. $\langle V \rangle^2$ shows no change due to this fluctuations but a correction comes from $\langle V^2 \rangle \sim g_1^2 (1 - I(f)) (\langle x_{bulk}^2 \rangle + \langle \delta x_{bulk}^2 \rangle) + \sum_{\alpha} I_{\alpha} g_2^2 (\langle x_{\alpha}^2 \rangle + \langle \delta x_{\alpha}^2 \rangle)$. The extra correction to resistivity it adds:

$$\delta\rho(T)_f \sim g_1^2 (1 - I(f)) \langle \delta x_{bulk}^2 \rangle + g_2^2 (I_l \langle \delta x_l^2 \rangle + I_m \langle \delta x_m^2 \rangle + I_h \langle \delta x_h^2 \rangle) \quad (12)$$

With $\langle \delta x_m^2 \rangle = 6 \langle \delta x_h^2 \rangle$ and $\langle \delta x_l^2 \rangle = \langle \delta x_h^2 \rangle = \langle \delta x_{bulk}^2 \rangle = \delta x^2$, we have

$$\delta\rho(T)_f \sim g_2^2 (I_l + 6I_m + I_h) \delta x^2 + g_1^2 (1 - I(f)) \langle \delta x^2 \rangle \quad (13)$$

The standard deviation $\delta x^2 \propto T = a \cdot T$ (Fig 4(d) in main paper), a being a constant.

$$\delta\rho(T)_f = a g_1^2 \langle \delta x^2 \rangle + a g_2^2 (I_l + 6I_m + I_h) \cdot T \quad (14)$$

To eliminate the dependence of a we normalize $\delta\rho(T)_f / \delta\rho(T, f = 0)$ and the linearity coefficient A comes out to be:

$$A \sim \frac{g_1^2 (1 - I(f)) + g_2^2 (I_l + 6I_m + I_h)}{g_1^2} \quad (15)$$

Comparing with numerical results

We estimated ρ_0 and A (via $\delta\rho(T)$) using perturbative analysis. In Fig.8 we plot these two quantities as a function of f against the exact numerical values. In 8(a) we plot the resistivity ρ_0 normalized by $\rho_0(f = 0.05)$. In Fig.8(b) we plot $A(f)$. Both these results matches quite well with the numerical exact results.

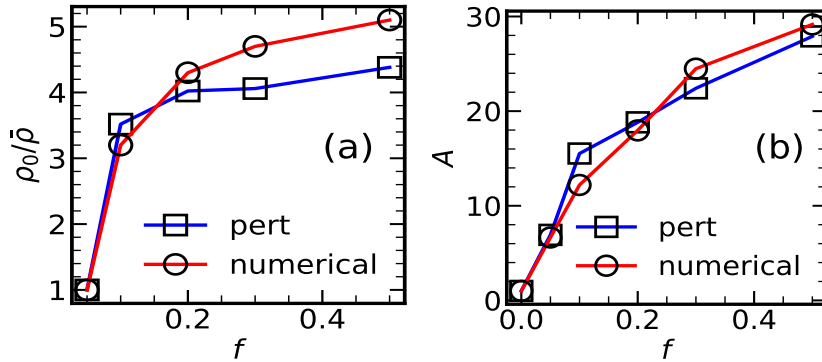


FIG. 8. Comparison of perturbative estimates and exact numerical values. Figure (a) shows the resistivity ρ_0 normalized by $\rho_0(f = 0.05)$ as a function of f . Figure (b) displays the coefficient $A(f)$.

VII. EFFECT OF PARAMETER VARIATION

variation of g_2

In Fig.9., we plot the resistivity $\rho(f = 0.5, T)$ at $f = 0.5$ for two different g_2 values (1.4 and 1.6). Notice, the ratio of zero temperature resistivity for these two different g_2 values is $\rho(T = 0, g_2 = 1.6)/\rho(T = 0, g_2 = 1.4) \sim 7$. The linear coefficient λ can be extracted ($\rho(T) \sim \rho_0 + \lambda T/t_{hop}$) and $\lambda(g_2 = 1.6)/\lambda(g_2 = 1.4) = 2.5$.

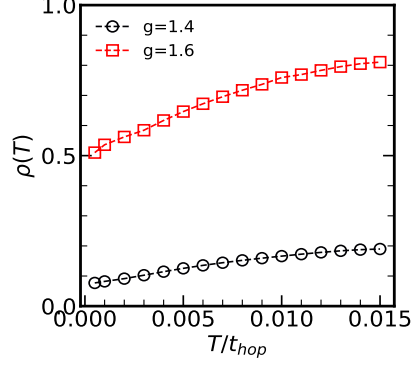


FIG. 9. The effect of varying g_2 values on $\rho(T)$ is investigated. Calculations are performed for $g_2 = 1.4$ and $g_2 = 1.6$.

Effect of onsite potential μ_i

Till now we did not consider the charge transfer between Au-Ag. In a simplified picture this would be equivalent to introducing an on-site term $-\sum_i \mu_i n_i$ to the Hamiltonian where μ_i is set to chemical potential μ_{Ag} (μ_{Au}) for Silver (Gold) sites. We consider this in the following calculation and set $\mu_{Au} - \mu_{Ag} = 0.5t_{hop}$. In Fig.10(a), we plot the density map n_i for one such configuration at $f = 0.5$ and $T/t_{hop} = 10^{-5}$. This shows the net charge is transferred from the Ag sites to Au sites. The resistivity as a function of temperature $\rho(T)$ is plotted in Fig.10(b) for three different f -values which shows trend similar to the case with out $m\mu_i$.

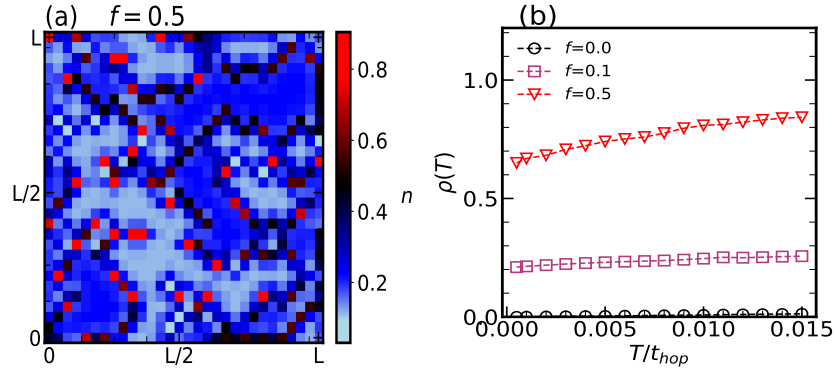


FIG. 10. (a) Density map n_i for a configuration with charge transfer between Au and Ag sites at $f = 0.5$ and $T/t_{hop} = 10^{-5}$. The charge transfer is modeled by setting $\mu_{Au} - \mu_{Ag} = 0.5t_{hop}$. (b) Resistivity as a function of temperature $\rho(T)$ is plotted for three different f -values.